Machine Perception based on Eddy Current for Physical Field Reconstruction of Conductivity and Hidden Geometrical Features

Min Li, and Kok-Meng Lee, Fellow, IEEE

Abstract— This article presents a new machine perception method based on eddy current (EC) effects to reconstruct physical fields (Eddy current field, electrical-conductivity field and hidden geometrical features) of a nonferrous material commonly encountered in intelligent manufacturing using one-time finite magnetic flux density (MFD) measurements. An analytical model for EC testing system with conductor discretization is established and expressed in state-space representation. Two improvements (physical constraints and adaptive element refinement) are developed and integrated into the system model. The measurement models of physical fields using discrete MFD measurements are linearly established, reducing the physical field reconstruction to a linear inverse problem for solving using Tikhonov regularization method. The EC-based machine perception is numerically illustrated by reconstructing the eddy-current density field, conductivity field and hidden geometrical features of aluminum plates. Additionally, the effects of element refinement, physical constraints and sensor configurations on the reconstruction results are analyzed numerically. Using an experimental prototype consisting of an air-cored electromagnet and a two-dimensional array of magnetic sensors with associated electronics, the effectiveness of the machine perception method and the accuracy of the reconstructed physical field are demonstrated experimentally.

Index Terms— Eddy-current testing, inverse problem, physical field reconstruction, Tikhonov regularization.

ACHINE perception and smart sensing are attracting more and more attention in many research fields, and are in exponentially growing demand for intelligent manufacturing in the past two decades. Because of stringent requirements and complex environments (such as workpiece deformation, cutting force vibration, thermal effects and residual stresses), highquality manufacturing with superior service capability has been challenging when machining special workpieces (for example, compressor disks and casings in aircraft engines with thinwalled shape [1][2]) or encountering newly developed manufacturing, such as the metallic-additive-manufacturing. Especially for the metallic-additive-manufacturing, most of the

defined theory, and insensitivity to oil or other media), EC sensors are well suitable for nondestructive testing [5][6] and for multi-target sensing in intelligent manufacturing [7]. Instead of analyzing the unmeasurable EC field, traditional methods of EC testing directly establishes the relationship of the desired parameters and measurable EC effects, such as characteristic impedance of the excitation coil [8][9], the voltage of a secondary or receiver coil [10][11], and the magnetic field generated by EC [12][13]. For instance, electrical conductivity estimation is one common application using EC technologies, I. Introduction which has the potential for the nondestructive evaluation of multiple material properties (such as subsurface residual stresses [14][15]). There are two primary types of EC-based methods for conductivity estimation based on the coil excitation: 1) frequency domain analysis using sinusoidal excitation [8][16], and 2) time domain analysis using pulsing

intelligent manufacturing.

Manuscript received August 1, 2018; revised March 12, 2019; accepted April 7, 2019. This work was supported in part by the National Science Foundation under Grant CMMI-1662700.

M. Li is with the Department of Mechanical and Civil Engineering, Minnesota State University, Mankato, MN 56001 USA (e-mail: min.li@ mnsu.edu).

K. -M. Lee is with the George W. Woodruff School of Mechanical Engineering, Georgia Institute of Technology, Atlanta, GA 30332 USA (e-mail: kokmeng.lee@me.gatech.edu).

transient excitation [17][18]. Another good application is the

detection of internal defects or non-conductive buried materials

(such as embedded sensors in a 3D-printed product) which can

be interpreted as hidden geometrical features. Different from

the conductivity estimation, most of the methods for defect

detection [19][20] are based on time-domain analysis using

pulsing transient excitation. The hidden geometrical features

critical problems focus on process reliability, finished-part geometries and material properties, which require layer by layer

defect detection as well as post-processing precision machining

[3][4]. Real-time estimation of the geometry and material

properties, defect detection (including the detection of internal

porosity, crack, residual stress and delamination [3] [4])

between layers are needed to be performed within large areas

or volumes. The effectiveness of the real-time parameter

sensing and process monitoring dictates the success of

Eddy current (EC) induced inside the electrical conductor

due to the presence of a changing magnetic field works as

media, which has the ability to transmit the properties of

conductors, such as location, geometry and electrical and

magnetic properties. Since magnetic field has many attractive

characters (such as great penetration, fast response, well

are classified or identified by relating the transient specifications (such as rise-time, peak-time) to the corresponding patterns of surface- and/or subsurface-features. Recently, by analyzing the thermal effects of the eddy current in time and frequency domain, EC thermography [21][22] has been developed for internal defect detection.

EC technologies have been widely used. However, most traditional EC testing methods estimate or measure a parameter at discrete points or over a small area. For applications (such as metallic-additive-manufacturing) requiring detection and measurement over a large area or volume, sensor probes need to scan the whole area, which is time-consuming and could dramatically lower manufacturing efficiency [9][11].

Existing EC methods are generally single-purpose (mostly designed based on high-frequency impedance measurements to estimate either the displacement or conductivity) using a lumped parameter approach; as a result, they are inefficient particularly involving large area/volume and/or multipleparameter measurements. As a physical quantity, eddy- current density (ECD) has been effectively used to describe the EC distribution over a target region of interest. In [7], an in-depth parametric study based on the relationship between a harmonically generated ECD field and material/geometrical properties demonstrates that several parameters can be simultaneously determined from measured ECD fields. The estimated ECD field not only can be used to verify the estimated conductivity and internal defect with the field density and pattern, but also monitor/visualize the EC stimulation used in medical and biological fields [23].

To overcome the limitations of conventional single-purpose EC sensors, this paper proposes an effective means to measure or detect the targeted parameters (or physical fields) of interests within a relatively large area/volume with one-time measurement. As an alternative machine perception based on EC effects and physical field reconstruction for manufacturing applications, the proposed method has potentials to integrate multi-functions in a compact sensor for estimating or detecting desired parameters within a large area/volume using one-time measurements. The remainder of the paper offers the following:

- An analytical model for an EC-based sensing system with conductor discretization is formulated in state-space representation. Two improvements, physical constraints and adaptive element refinement, are developed and integrated into the system model.
- The measurement models of physical fields relating the physical parameters and the discrete magnetic flux density (MFD) measurements are derived, which reduce the physical field reconstruction to a linear inverse problem for solving using Tikhonov regularization method.
- The effectiveness and accuracy of the reconstruction method are demonstrated numerically. The conductivity and hidden geometrical feature of aluminum plates and the ECD field are estimated. Meanwhile, the effects of element refinement, physical constraints and sensor configuration on the reconstruction results are analyzed numerically.
- An experimental setup consisting of a sensor array, an air-

cored electromagnet (EM) and associated hardware is utilized to reconstruct the physical fields (conductivity and hidden geometrical feature, and ECD field).

II. PHYSICAL FIELD RECONSTRUCTION

Figure 1 illustrates a method to reconstruct the ECD field induced in a non-ferrous metal conductor from a set of N_M MFD measurements, from which the distribution of the electrical conductivities and geometrical features in the conductor are characterized. The conductor, in which the EC is induced by a time-varying source, is discretized into N_E elements. The i^{th} element (volume v_i and electrical conductivity σ_i) and m^{th} sensor are located by the displacement vectors, \mathbf{r}_i and \mathbf{r}_m , respectively, where $i = 1, 2... N_E$ and $m = 1, 2... N_M$. The external sources for inducing the EC may or may not be a part of the measuring system but are known or can be pre-calibrated. As the source-MFD can be subtracted from the sensor output, the m^{th} measurement $\beta_m (\in \mathbb{R}^{3\times 1})$ represents the MFD generated at the location of the m^{th} sensor by EC in all N_E elements.

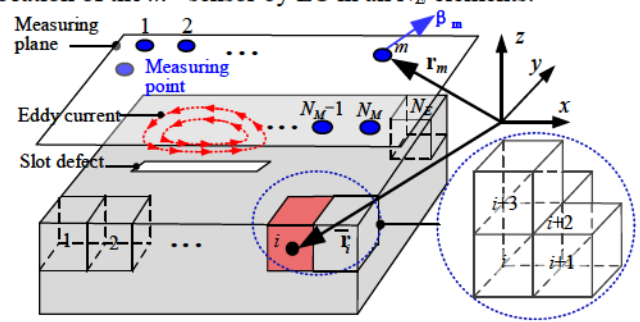


Fig. 1 Schematics of physical field reconstruction

A. System Model

The system is magneto-quasi-static with negligible displacement current and $\omega L \ll 1/\sqrt{\mu\varepsilon} \approx 3\times 10^8\,\mathrm{m/s}$ where ω is the system frequency, (ε, μ) are the (permittivity, permeability) of the conductor that obeys Ohm's law; and L is the characteristic length. The ECD field can be written in matrix-vector form (1a) where its i^{th} elemental ECD \mathbf{j}_i (contributed by the MFD generated by the source and by the self/mutual induction among N_E elements) can be expressed in terms of vector potentials in (1b) [24]:

$$\mathbf{J} = \begin{bmatrix} \mathbf{j}_1 & \cdots & \mathbf{j}_i & \cdots & \mathbf{j}_{N_E} \end{bmatrix}^{\mathrm{T}}$$
 (1a)

where
$$\mathbf{j}_{i} = -\sigma_{i} \nu_{i} \frac{\partial}{\partial t} \left(\mathbf{\phi}(r_{i}, t) + \mu_{0} \sum_{k=1}^{N_{E}} \frac{1}{4\pi |\mathbf{r}_{i} - \mathbf{r}_{k}|} \mathbf{j}_{k} \right);$$
 (1b)

and μ_0 is the magnetic permeability in free space, r_k is the position vector of the k^{th} element. Similarly, the EC-generated MFD measurements are given in (2a) in matrix form where the m^{th} measured MFD β_m can be derived from the curl of the vector potential [24]:

$$\boldsymbol{\beta} = \begin{bmatrix} \boldsymbol{\beta}_1 & \cdots & \boldsymbol{\beta}_m & \cdots & \boldsymbol{\beta}_{N_M} \end{bmatrix}^{\mathrm{T}}$$
 (2a)

$$\boldsymbol{\beta}_{m} = -\sum_{i=1}^{N_{E}} \left\{ \frac{\mu_{0}}{4\pi \left| \mathbf{r}_{m} - \mathbf{r}_{i} \right|^{2}} \left[skew \left(\frac{\mathbf{r}_{m} - \mathbf{r}_{i}}{\left| \mathbf{r}_{m} - \mathbf{r}_{i} \right|} \right) \right] \mathbf{j}_{i} \right\}$$
(2b)

In (2b), the square matrix [skew (e)] denotes the skew matrix of the unit vector e.

In physics, the induced EC must satisfy the constraints imposed by the boundaries and the principle of charge conservation. The former accounts for the fact that EC cannot pass through a non-electric element and must satisfy the boundary constraint ($\mathbf{j}_i \cdot \mathbf{n} s_n = 0$) where \mathbf{n} is the unit normal to the boundary surface area s_ℓ ; for simplicity, we define the subscript $\ell = x, y, z$. In matrix form,

boundary constraint (BC):
$$[\mathbf{H}_{\mathbf{B}}]\mathbf{J} = 0$$
 (3a)

For a system of the N_E elements consisting of N_B boundary elements in (3a), the row vector of $[\mathbf{H_B}] \in \mathbb{R}^{N_B \times 3N_E}$ has the form given by (3b) where the i^{th} element is a boundary element:

$$\begin{bmatrix} \mathbf{0} (\in \mathbb{R}^{1 \times 3(i-1)}) & s_{\ell} \mathbf{n}^{\mathsf{T}} & \mathbf{0} (\in \mathbb{R}^{1 \times 3(N_E - i)}) \end{bmatrix}$$
(3b)

Without loss of generality, consider a hexahedron element (with surface areas s_{ℓ} and unit normal \mathbf{e}_{ℓ}) for illustrating the *principle* of charge conservation that implies $\nabla \cdot \mathbf{j}_i = 0$. The i^{th} element must satisfy the continuity equation:

$$(\mathbf{j}_{i+1} - \mathbf{j}_i) \cdot \mathbf{e}_x s_x + (\mathbf{j}_{i+2} - \mathbf{j}_i) \cdot \mathbf{e}_y s_y + (\mathbf{j}_{i+3} - \mathbf{j}_i) \cdot \mathbf{e}_z s_z = 0$$

Similarly,

charge conservation:
$$[\mathbf{H}_{\mathbf{C}}]\mathbf{J} = 0$$
 (4a)

The row vector of $[\mathbf{H}_C]$ ($\in \mathbb{R}^{N_C \times 3N_E}$) where N_C ($=N_E - N_B$) has the form given by (4b) where the i^{th} element is a non-boundary element:

$$\begin{bmatrix} \mathbf{0}(\in \mathbb{R}^{1\times 3(i-1)}) & -\mathbf{s}^{\mathrm{T}} & \mathbf{s}_{x}^{\mathrm{T}} & \mathbf{s}_{y}^{\mathrm{T}} & \mathbf{s}_{z}^{\mathrm{T}} & \mathbf{0}(\in \mathbb{R}^{1\times 3(N_{E}-i-3)}) \end{bmatrix}$$
(4b)

where
$$\mathbf{s}^{\mathrm{T}} = \begin{bmatrix} s_x & s_y & s_z \end{bmatrix}$$
 and $\mathbf{s}_{\ell}^{\mathrm{T}} = \mathbf{s}^{\mathrm{T}}$ (with $s_{\neq \ell} = 0$).

For describing the ECD and its corresponding MFD of the system with N_E conductor elements, N_M observations and $(N_B$ boundary and N_C continuity) constraints, the time-invariant state and output equations can be derived from (1) to (4). In state-space representation,

State equation:
$$\dot{\mathbf{J}} = [\mathbf{A}]\mathbf{J} + [\mathbf{B}](d\mathbf{U}/dt)$$
 (5a)

where
$$\mathbf{U} = \left[\mathbf{\phi}(\mathbf{r}_1, t) \quad \cdots \quad \mathbf{\phi}(\mathbf{r}_i, t) \quad \cdots \quad \mathbf{\phi}(\mathbf{r}_{N_E}, t) \right]^{\mathrm{T}}$$
 (5b) subject to constraints (3) and (4).

Output equation:
$$\beta = [C]J$$
 (6a)

where [C] consists of $N_M \times N_E$ submatrices with its mi^{th} (3×3) submatrix given by

$$\left[C_{mi}\right] = \frac{\mu_0}{4\pi \left|\mathbf{r}_m - \mathbf{r}_i\right|^2} \left[skew\left(\frac{\mathbf{r}_m - \mathbf{r}_i}{\left|\mathbf{r}_m - \mathbf{r}_i\right|}\right)\right]$$
(6b)

The ECD field **J** can be estimated from finite measurements with (6) using an observer or calculated analytically from (5) for a given time-varying input $(d\mathbf{U}/dt)$ if the system matrix [A] and input matrix [B] are known:

$$[\mathbf{A}] = -[\varsigma]^{-1}([\mathbf{P}] + [\dot{\varsigma}]); \quad [\mathbf{B}] = -\mu_0^{-1}[\varsigma]^{-1}$$
 (7a,b)

In (7a), [P] is a diagonal matrix consisting of N_E non-zero 3×3 submatrices, where the i^{th} submatrix is given by

$$[\mathbf{P}_{ii}] = (\mu_0 \sigma_i \nu_i)^{-1} [\mathbf{I}_{3\times 3}]$$
 (7c)

where $[\mathbf{I}_{3\times3}]$ is a 3×3 identical matrix. Similarly, $[\varsigma]$ in (7a, b) are expressed as $N_E \times N_M$ submatrices with its ik^{th} (3×3) submatrix given by $[\varsigma_{ik}] = (4\pi |\mathbf{r}_i - \mathbf{r}_k|)^{-1} [\mathbf{I}_{3\times3}]$. In (7a, b), $[\mathbf{A}]$ depends on $[\mathbf{P}]$ that accounts for the non-uniformity of the material properties and geometrical features $(\sigma_i \ v_i)$, and the time-derivatives of the motion due to any deformation and deflection of the conductor; $[\mathbf{B}]$ depends on the geometry feature only for a nonferrous conductor with constant μ_0 but neither the time-derivative nor material property. The other three matrices depend on the geometry feature only.

B. Formulation of Measurement Models

Without loss of generality for simplicity in illustration, the following assumptions are made in formulating measurement models for manufacturing inspection:

- The specified geometrical details of the WP being processed are known in advance. Furthermore, the sensing speed is sufficiently fast that the shape of the workpiece (WP) can be assumed approximately constant.
- 2) The WP is stationary ($[\dot{\varsigma}]=0$); and its material is isotropic.
- 3) The external source $\dot{\mathbf{U}}$ inducing the ECD in the metallic plate (with known exterior geometry) is known.

With these assumptions, the state-space equations provide a basis to determine the desired output β_0 for detecting hidden non-conductive geometrical features (or defects), and estimating the distribution of the conductivity fields. Once the hidden geometrical features and conductivity distribution are completely known, the ECD field **J** can be reconstructed from the state equations (5a, b).

Alternatively, the measurement models are formulated as inverse problems. Unlike the forward kinematics (5a, b) where the solutions to J can only be solved with known [A] and [B] for the given material and geometrical properties, the inverse solutions deduce the target fields directly from the measurement β of the MFD generated by EC. The formulation is best illustrated by the following three application scenarios as described in Subsections B.1, B.2 and B.3:

- Detecting non-conductive geometrical features in conductor with approximately known conductivity (*B.1*)
- Estimating the electrical conductivity in nonferrous conductor with known geometry (B.2).
- Reconstructing the ECD field in conductor with known geometry and conductivity (B.3).

B.1 Hidden non-conductive geometric features detection

The measurement model for reconstructing the interior geometry in conductor with an approximately known conductivity is formulated in (8) where $\hat{Y}_1(=\beta-\beta_0)$ defines the deviation of the measured β from the desired β_0 and η_1 accounts for errors in the measured data:

$$\hat{\mathbf{Y}}_{1} = [\mathbf{Q}]\mathbf{T} + \mathbf{\eta}_{1} \tag{8a}$$

In (8a), each element in the probability vector $\mathbf{T}(\in \mathbb{R}^{N_E \times 1})$ has a value between 0 (conductive) and 1 (non-conductive)

indicating the likelihood that the element is electrically conductive; and

$$[\mathbf{Q}](\in \mathbb{R}^{N_M \times N_E}) = \begin{bmatrix} \mathbf{q}_1 & \mathbf{q}_2 \cdots & \mathbf{q}_i \cdots & \mathbf{q}_{N_E} \end{bmatrix}$$
(8b)

$$\mathbf{q}_{i} = \begin{bmatrix} \mathbf{\breve{\beta}}_{i1} \cdots \mathbf{\breve{\beta}}_{im} & \cdots \mathbf{\breve{\beta}}_{iN_{M}} \end{bmatrix}^{\mathrm{T}} - \mathbf{\beta}_{0}$$
 (8c)

In (8b), the sensitivity matrix [Q] with its column vector \mathbf{q}_i given by (8c) can be pre-calculated using (5) and (6), where $\breve{\boldsymbol{\beta}}_{im}$ is the theoretically expected m^{th} MFD sensor output of the specified WP except the i^{th} element is nonconductive. For the subsequent conductivity estimation and the ECD field reconstruction, a threshold (normally the average of all elements) will be applied to determine the corresponding elements are occupied or not.

B.2 Conductivity estimation

In most applications, the targeted conductivity of the material is a designed value (in manufacturing, for example) or approximately known. The measured β is a nonlinear function of the N_E elemental conductivities,

$$\beta(\sigma)$$
 where $\sigma = \begin{bmatrix} \sigma_1 \cdots & \sigma_i & \cdots \sigma_{N_E} \end{bmatrix}^T$.

For small deviations about the desired values $(\bar{\sigma}, \beta_0)$, a linearized measurement model to reconstruct the conductivity field is formulated in (9) where $\hat{\sigma} = \sigma - \bar{\sigma}$ and η_2 accounts for errors in the measured deviation $\hat{Y}_2(=\beta - \beta_0)$:

$$\hat{\mathbf{Y}}_2 = \hat{\boldsymbol{\beta}} = [\mathbf{G}]\hat{\boldsymbol{\sigma}} + \boldsymbol{\eta}_2 \tag{9a}$$

In (9),
$$\left[\mathbf{G}\right] = \left[\partial \mathbf{\beta} / \partial \mathbf{\sigma}\right]^{\mathrm{T}}$$
 (9b)

$$\frac{\partial \mathbf{\beta}}{\partial \sigma_{\cdot}} = \frac{1}{\Delta \sigma} \left(\begin{bmatrix} \tilde{\mathbf{\beta}}_{i1} \cdots & \tilde{\mathbf{\beta}}_{im} & \cdots \tilde{\mathbf{\beta}}_{iN_{M}} \end{bmatrix}^{T} - \mathbf{\beta}_{0} \right)$$
(9c)

The Jacobian matrix [G] with its i^{th} column given by (9c) can be pre-calculated using (5) and (6), where $\tilde{\beta}_{im}$ represents the m^{th} MFD measurement of the specified WP except the i^{th} element with conductivity ($\bar{\sigma} + \Delta \sigma$).

B.3 Reconstruction of ECD field

The reconstruction of the ECD field **J** induced in a nonferrous metallic plate (with known geometry) is essentially as an inverse problem in (10) which requires no knowledge of material properties:

$$\mathbf{Y}_{3} = \begin{bmatrix} \mathbf{\beta} \\ \mathbf{0} \end{bmatrix} = \begin{bmatrix} \mathbf{C} \\ \mathbf{H}_{\mathbf{B}} \\ \mathbf{H}_{\mathbf{C}} \end{bmatrix} \mathbf{J} + \mathbf{\eta}_{3}$$
 (10)

In (10) where N_B boundary constraints and N_C continuity equations are augmented in the output equation (6), \mathbf{Y}_3 is the measurement vector; and $\mathbf{\eta}_3$ accounts for errors in the measured data. For cases with no BCs, the matrix $[\mathbf{H}_B]$ in (10) is zero. However, (10) cannot be used to reconstruct \mathbf{J} when the conductor has unknown (hidden) geometric features and thus $[\mathbf{H}_B]$, $[\mathbf{H}_C]$ and $[\mathbf{C}]$ are not defined.

All the three measurement models (8a), (9a), and (10) described above can be written in generalized form as shown in

(11) to determine **X** from the measurement vector $\mathbf{Y} (\in \mathbb{R}^{n \times 1})$ and given $[\mathbf{K}]$ in the presence of noise $\mathbf{\eta}$:

$$\mathbf{Y} = \left[\mathbf{K} \right] \mathbf{X} + \mathbf{\eta} \tag{11}$$

For a noise-free system with nonsingular [K] and $n \ge m$, (11) can be solved using pseudoinverse (12):

$$\mathbf{X} = [\mathbf{R}]\mathbf{Y} \text{ where } [\mathbf{R}] = ([\mathbf{K}]^{\mathsf{T}}[\mathbf{K}])^{-1}[\mathbf{K}]^{\mathsf{T}}$$
 (12a,b)

However, n < m in practice when reconstructing a physical field from limited measurement data. As a result, **[K]** becomes increasingly ill conditioned as measurement cost increases. The pseudoinverse solutions (12) fail as the noise η in Y may be greatly amplified.

C. Inverse Solutions Based on Tikhonov Regularization

Tikhonov regularization [25] commonly used in machine learning is employed to solve the ill-posed problem (13):

$$\mathbf{X}_{\alpha} = [\mathbf{R}_{\alpha}] \mathbf{Y} \text{ where } [\mathbf{R}_{\alpha}] = ([\mathbf{K}]^{\mathsf{T}} [\mathbf{K}] + \alpha [\mathbf{I}])^{-1} [\mathbf{K}]^{\mathsf{T}}$$
 (13a, b)

In (13b), α (with range [0, 1]) is the regularization parameter to control noise effects and prevent overfitting; and [**K**] is a known real-valued matrix and has a singular value decomposition (SVD) with strictly positive decreasing singular values s_i :

$$[\mathbf{K}] = [\mathbf{F}] \left[\operatorname{diag}(s_i) \right] [\mathbf{G}]^{\mathsf{T}}$$
(14)

In (14), **F** and **G** consist of column vectors, \mathbf{f}_i and \mathbf{g}_i , respectively. The error \mathbf{e}_{α} (= \mathbf{X}_{α} - \mathbf{X}) consists of regularization truncation error $\hat{\mathbf{e}}_{\alpha}$ and noise amplification error $\tilde{\mathbf{e}}_{\alpha}$ defined as

$$\hat{\mathbf{e}}_{\alpha} = ([\mathbf{R}_{\alpha}][\mathbf{K}] - [\mathbf{I}])\mathbf{Y} \text{ and } \tilde{\mathbf{e}}_{\alpha} = [\mathbf{R}_{\alpha}]\mathbf{\eta}$$
 (15a, b)

Very small α will result in inadequate filtering of the noise and highly oscillatory solution. On the other hand, overly smooth solutions would filter out most solution components. In this work, α trades off between noise filtering and solution smoothness using an L-Curve graphical method [26][27], which requires no prior information about sensor noise. The regularization for the inverse solutions should satisfy the requirement that $\tilde{\bf e}_{\alpha} \to 0$ when ${\bf \eta} \to 0$. Substituting (14) and

 $[\mathbf{R}_{\alpha}]$ from (13b) into (15a, b) lead to

$$\hat{\mathbf{e}}_{\alpha} = \sum_{i=1}^{n} \left(w_{\alpha} \left(s_{i}^{2} \right) - 1 \right) \left(\mathbf{f}_{i}^{\mathsf{T}} \mathbf{J} \right) \mathbf{g}_{i}$$
 (16a)

$$\tilde{\mathbf{e}}_{\alpha} = \sum_{i=1}^{n} w_{\alpha} \left(s_{i}^{2} \right) s_{i}^{-1} \left(\mathbf{f}_{i}^{\mathrm{T}} \mathbf{\eta} \right) \mathbf{g}_{i}$$
 (16b)

In (16a, b), the Tikhonov filter function

$$w_{\alpha}(s^2) = \frac{s^2}{s^2 + \alpha} \to 1 \text{ as } \alpha \to 0; \ \hat{\mathbf{e}}_{\alpha} \to 0$$
 (16c)

Since $w_{\alpha}(s^2)s^{-1} \le \alpha^{-1/2}$, α is chosen to have the form (17a) in terms of the error level δ defined in (17b):

$$\alpha = \delta^p$$
 where $\delta = \|\mathbf{\eta}\| > 0$ and $0 (17a, b, c)$

where $\| \cdot \|$ denotes the standard Euclidean norm. Equations (16b) and (17b) lead to (17d):

$$\tilde{\mathbf{e}}_{\alpha} \le \alpha^{-1/2} \delta = \delta^{1-p/2} \tag{17d}$$

The above implies that the requirement $\tilde{\mathbf{e}}_{\alpha} \to 0$ as $\delta \to 0$ can be guaranteed with (α, p) given by (17a, c).

D. Effects of Element Sizes on Regularization Accuracy

The accuracy and effectiveness of the reconstruction based on Tikhonov regularization depend on the number of state variables for a given sensor system. To improve the accuracy in reconstructing the eddy current while maintaining a manageable number of state variables, the elements are distributed based on two criteria on each elemental ECD:

$$\|\mathbf{j}_{i}\| \ge k \|\mathbf{j}\|_{\max}$$
 and $\frac{l_{i}}{\|\mathbf{j}_{i}\|} \left\| \frac{\partial \mathbf{j}_{\ell}}{\partial \ell} \right\| \ge g$ (18a,b)

where $\ell = x, y, z$. The 1st criterion compares $\|\mathbf{j}_i\|$ with a predetermined threshold $k \|\mathbf{j}_{\text{max}}\|$ where 0 < k < 1 based on the maximum ECD j_{max} , whereas the 2^{nd} criterion compares its gradient against a pre-determined threshold g, upon which element i is divided evenly into 2, 4 or 8 elements in the corresponding ℓ directions as illustrated in Fig. 2(a).

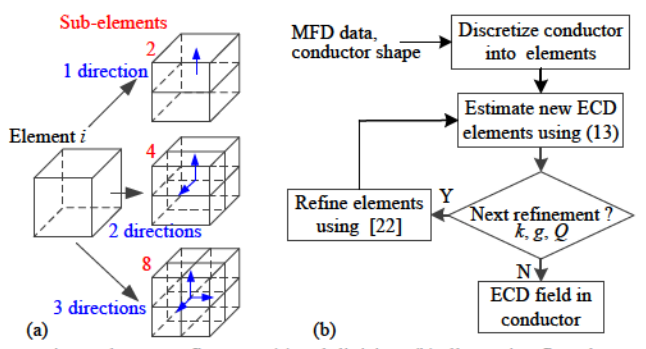


Fig. 2 Element refinement (a) Subdivision. (b) Illustrative flowchart

Since the element refinement will change the state vector dimension, which in terms will affect the choice of the regularization parameter α , the elements are sized such that the magneto-quasi-static conditions mathematically expressed in (19) and noise error condition (17c) are not violated:

$$l < L \ll \omega^{-1} \left(\mu \varepsilon\right)^{-1/2} \tag{19}$$

$$0$$

The procedure consisting of the following steps for refining the elements is graphically illustrated in Fig. 2(b): Given the MFD data and conductor shape, Step 1 begins with evenly spaced elements. Next, the elemental variables of the field to be reconstructed are estimated using (13a) integrated with proper constraints in the 2^{nd} step. In the 3^{rd} step, given k, g and the maximum iteration Q, the refinement criteria (18a, b) are examined to determine whether the elements should be further sub-divided. The 2nd and 3rd steps are repeated until the criteria are met or the algorithm exceeds O.

III. RESULTS AND DISCUSSION

The effectiveness of the inverse solutions to field reconstruction (13a) based on Tikhonov regularization (13b) has been investigated numerically and experimentally. Sinusoidal MFD fields are used to induce eddy-current in the conductor. For model validation and parametric studies, the

induced ECD and its corresponding MFD are simulated numerically. For verification of the reconstructed distribution, the actual conductivity distribution was experimentally measured by a commercial conductivity gauge (Sigma 2008A, precision: ± 1%). The algorithms were written in MATLAB and computed on a desktop PC (Intel Core i7-7700, 3.60-GHz CPU, 16-GB RAM, 64-b OS). To facilitate comparisons with published solutions, the harmonic solutions are derived from the system equations, $\mathbf{J} = \begin{bmatrix} \mathbf{J}_{Re} & \mathbf{J}_{Im} \end{bmatrix}^T$ and $\boldsymbol{\beta} = \begin{bmatrix} \boldsymbol{\beta}_{Re} & \boldsymbol{\beta}_{Im} \end{bmatrix}^T$ where the subscripts "Re" and "Im" refer to their respective real and imaginary parts:

$$\begin{bmatrix} [\mathbf{P}] + [\dot{\varsigma}] & -\omega[\varsigma] \\ \omega[\varsigma] & [\mathbf{P}] + [\dot{\varsigma}] \end{bmatrix} \begin{bmatrix} \mathbf{J}_{Re} \\ \mathbf{J}_{Im} \end{bmatrix} = \begin{bmatrix} 0 \\ -(\omega/\mu_0)\mathbf{U} \end{bmatrix}$$
(20a)

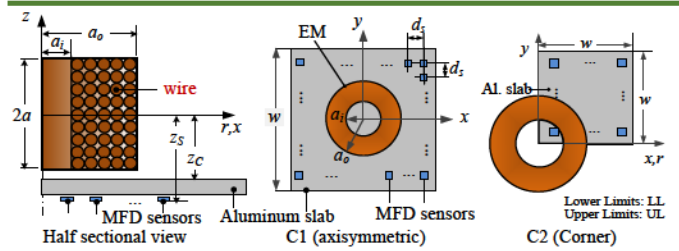
Subject to

$$\begin{bmatrix} \begin{bmatrix} \mathbf{H}_{B} \end{bmatrix} & \mathbf{0} \\ \mathbf{0} & \begin{bmatrix} \mathbf{H}_{B} \end{bmatrix} \end{bmatrix} \begin{bmatrix} \mathbf{J}_{Re} \\ \mathbf{J}_{Im} \end{bmatrix} = \mathbf{0} \text{ and } \begin{bmatrix} \begin{bmatrix} \mathbf{H}_{C} \end{bmatrix} & \mathbf{0} \\ \mathbf{0} & \begin{bmatrix} \mathbf{H}_{C} \end{bmatrix} \end{bmatrix} \begin{bmatrix} \mathbf{J}_{Re} \\ \mathbf{J}_{Im} \end{bmatrix} = \mathbf{0}$$

$$\beta = \begin{bmatrix} \boldsymbol{\beta}_{Re} & \boldsymbol{\beta}_{Im} \end{bmatrix}^{T} = \begin{bmatrix} \mathbf{C} \end{bmatrix} \begin{bmatrix} \mathbf{J} \end{bmatrix}$$
(20d, e)

The (Re, Im) parts of the ECD column vector **j**, defined in (1a) are given by $(j_{it}\cos\theta_{it}, j_{it}\sin\theta_{it})$ with amplitude j_{it} and phase $\theta_{i\ell}$ in $\ell(=x,y,z)$ directions. Similarly, the (Re, Im) parts of the column vector β_m defined in (2a) are given by $(\beta_{m\ell}\cos\varphi_{m\ell}, \beta_{m\ell}\sin\varphi_{m\ell})$ with amplitude $\beta_{m\ell}$ and phase $\varphi_{m\ell}$.

Table I illustrates the sensor system and lists the parametric



100-turn EM (a, a, a)	$(6.5, 7.7, 3.65)$ Sinusoidal input $(I_0 = 1A)$			
Aluminum slab	$\sigma = 2.16 \times 10^7 \text{ S/m}, z_C = -7.1$			
Configuration $(w \times w)$	C1 (60×60)	C2 (30×30)		
Sensors $(N_M; d_s, z_s)$	(15×15; 4, -12.5)	(11×11; 3, -12.5)		
Location (LL: d_s : UL)	-28: 4: 28	0: 3: 30		

Reconstruction simulation parametric values: C1; f = 1 kHz; h = 3 mmElement size (N_E) 2×2×3 (900) Conductivity C1 and C2; f = 1 kHz; h=1mm Element size (N_E) 2×2×1 (900) C1 and C2; f = 1 kHz; h=3mm

Initial element size (N_E) 6×6×3 (100) 3.75×3.75×3 (64) Refinement (k, Q, g) (0.1, 4, 30%)(0.1, 4, 30%)

FEA (COMSOL) simulation parameters for C2:

Simulation space (mm³): $60 \times 60 \times 60$ Total number of elements: 64268 Number of boundary elements: 3619

Minimum element quality: 0.2352



Feature

ECD

Table I illustrates the sensor system and lists the parametric values used in the simulations and experiments, where an EM (excited by a sinusoidal current with an amplitude I_o and frequency $\omega=2\pi f$) is placed above a conducting slab (Al specimen with an electrical conductivity of $\sigma=2.16\times10^7$ S/m [28]).

The skin depth $\delta = \sqrt{1/(\pi\mu_0 f \sigma)}$ (defined as the depth below the surface of the conductor at which the current density has fallen to e^{-1}) is used as a guide to select an excitation frequency f. Because the method requires only the EC to penetrate the plate thickness, the criterion that requires the skin-depth/platethickness ratio (δh) greater than unity ($\delta h \geq 1$) is set as a rule of thumb. In an industrial setting, the choice of an appropriate frequency is essentially a trade-off between the signal-to-noise ratio (SNR) and the skin -depth penetration; the former can be improved by means of high excitation frequency but too high a frequency will result in small EC penetration. To meet the criterion ($\delta/h \ge 1$) for the 3mm-thick Al ($\sigma = 2.16 \times 10^7$ S/m) specimen, the excitation frequency is equal or less than 1300 Hz. For the thin-plate applications illustrated in this paper, f =1 kHz was used for the 1mm- and 3mm-thick Al specimens in the simulations and experiments.

A. Numerical Investigation

Two Aluminum (Al) alloy configurations (denoted as C1 and C2 in Table I) are used to illustrate the inverse solutions (13b) for *geometrical feature detection* (8), *conductivity estimation* (9), and *ECD field reconstruction* (10):

- C1: The EM is placed at the center of a relatively large Al slab. Its induced EC field is 2D axisymmetric, for which analytical solutions [29][30] are available for verification.
- C2: The EM is placed at the corner of an Al slab. Since analytical solutions that generally neglect the boundary effects cannot be used to compute the induced ECD field, the ECD field is verified by comparing with finite element analysis (FEA) using commercial COMSOL software with the simulation parameters illustrated in Table I.

The MFDs at specified locations were calculated using analytical or FEA solution as "measurements".

A.1 Non-conductive Geometrical Feature Detection

The 1st set of results detect two common geometrical (cylindrical and slot) features in a 3mm-thick Al slab, where an eddy-current was induced in C1 (Table I) by a 1 kHz sinusoidal current flowing through the EM. The effects of sensor configurations (characterized by the ratio $d_s/l = 2$, 3 and 5, where l is the smallest dimension of the elements) on the solutions to the ill-posed inverse problem were numerically analyzed. The results are presented in Figs. 3(a) to 3(d) comparing three different types (through, interior and hidden-blind) of a 6mm-radius circular hole and a 20mm×2mm slot, which are located at (10mm, 10mm) and (0, -10mm) on the x-y plane.

The estimated errors of the feature location (x, y), the hole-radius r and the slot length b are summarized in Table II, where the errors of the parameter P(x, y, r, b) are defined as $|P_{\text{estimated}} - P_{\text{actual}}| / P_{\text{actual}}|$. As demonstrated in Fig. 3, the three

geometrical features can be successfully distinguished from the different thresholds of **T** values (≈ 1 yellow, 0.5 internal and hidden-blind). The estimation performance decreases as d_s/l increases (or with the smaller number of measurements), resulting in blurry edges.

Table II. % estimated errors of feature location (x, y) and size

Type	Through			Interior	Blind
d_s/l	5	3	2	2	2
Hole Loc.	4.37, 4.43	3.61,	2.93, 1.82	3.22, 2.59	3.62, 3.46
		3.53			
Radius	6.27	6.14	7.49	12.1	15.3
Slot Loc.	2.42, 12.2	3.19,	2.49, 11.8	2.56, 12.6	2.09, 10.23
		11.2			
Length b	13.1	8.27	4.27	4.93	5.35

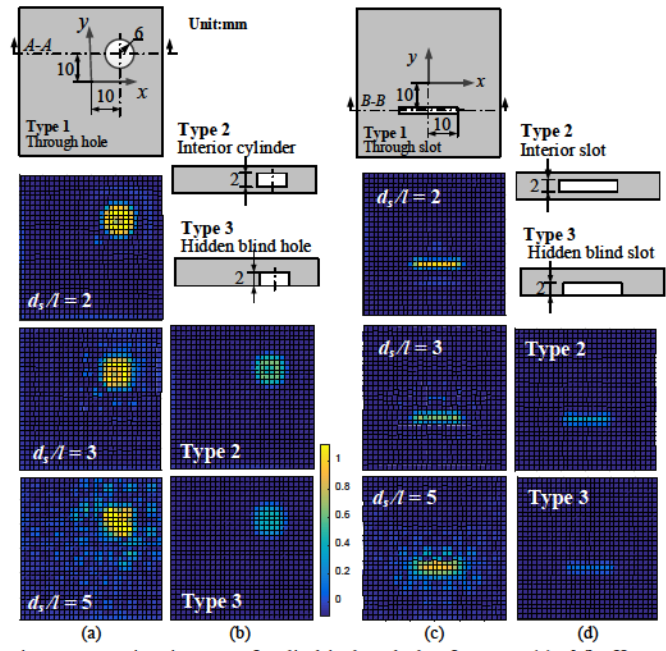


Fig. 3. Detection images of cylindrical and slot features. (a) d_s/l effect on reconstructed circular through-hole feature. (b) Effect of hidden hole types with $d_s/l = 2$. (c) d_s/l effect of on reconstructed rectangular through-slot feature. (d) Effect of hidden slot types with $d_s/l = 2$.

A.2 Conductivity estimation

The 2^{nd} set of simulations numerically estimates the conductivity distribution of a 1mm-thick Al slab with 1 kHz excitation current. The conductor is evenly divided into small (2mm×2mm×1mm) elements; and the sensors are evenly spaced with interval d_s =4mm. The "true" conductivity distribution of the plate is assumed to have a circular or an axisymmetric form commonly encountered in industry:

$$\frac{\sigma(x,y)}{\sigma_0} = 1 + q_o \left[\left(\frac{x}{w/2} \right)^2 + \left(\frac{y}{w/2} \right)^2 \right]$$
 (21)

where w=60mm; the aluminum conductivity σ_0 (= 2.16 × 10⁷S/m); and q_o is a constant that determines the variation of the preset conductivity distribution. The estimated results of two variations (q_o =0.3 and 0.03) in C1 and C2 are compared with the pre-set electrical conductivity in Figs. 4(a, b).

As shown in Figs. 4(a, b), the estimation curves, in general, follow the trend of the "true" conductivity, particularly when the variation is small. Some discrepancies can be seen in the case of large variation (q_o =0.3) in the region under the EM

center and that from the EM, where the eddy-current is relatively small. The effects of sensor spacing d_s/l on estimation errors defined as $|\sigma_{\rm est} - \sigma_{\rm preset}|/\sigma_{\rm preset}$ are shown in Fig. 4(c) where $q_o = 0.03$. The errors are within 0.3%, 3% and 4% of the preset σ for $d_s/l = 2$, 3 and 5 respectively.

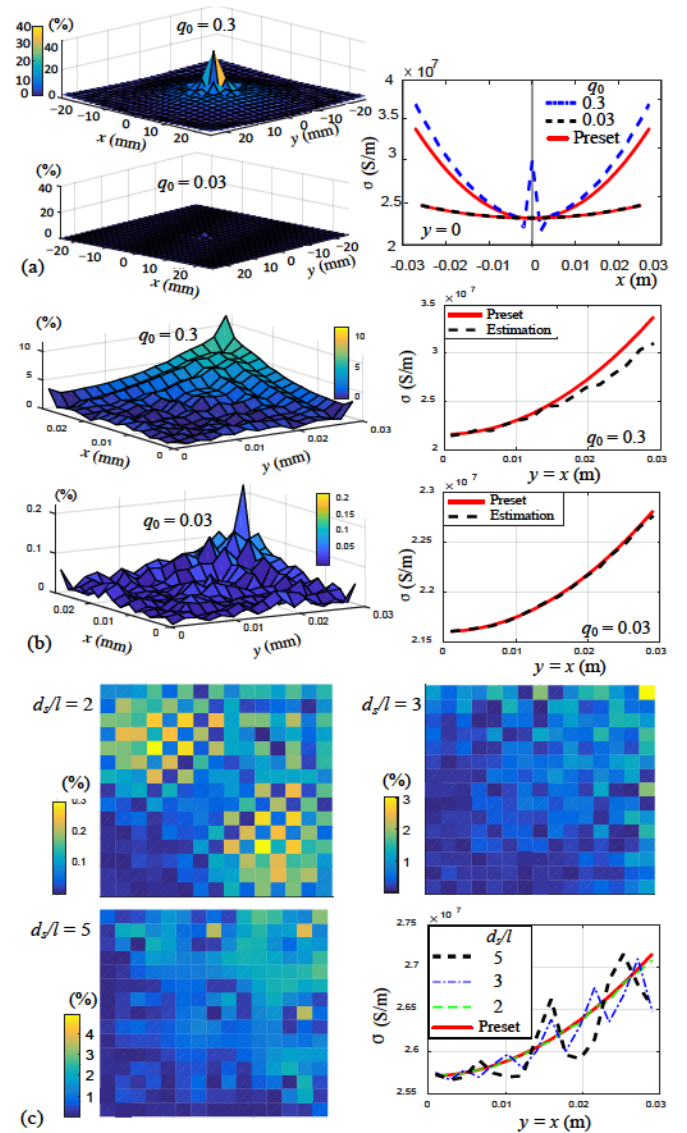


Fig. 4. Conductivity estimation. Comparison of q_o effect on (a) C1 without boundary effects and (b) C2 with boundary effects. (c) Effect of ratio d_z / l on C2 conductivity reconstruction errors.

A.3 ECD Field Reconstruction

The 3rd set of simulations numerically verifies (13a, b) for reconstructing ECD induced in a conductor, a 1mm-thick Al slab is illustrated as an example. For quantitative evaluation, the following % estimation error E_J is defined in (22) where \mathbf{J}_{true} is analytical or FEA solution.

%
$$E_J = 100 \frac{\left| \mathbf{J}_{\text{estimated}} \right| - \left| \mathbf{J}_{\text{true}} \right|}{\left| \mathbf{J}_{\text{true}} \right|}$$
 (22)

The objectives of the numerical investigation and their corresponding results are summarized as follows:

1) Validate of the adaptive refinement scheme:

The reconstructed ECD fields in C1 and C2 are presented in

Fig. 5(a, b), where the 1st and 2nd rows show the initial and final element distributions; and the 3rd row compares the reconstructed (Re and Im) parts of the ECD J_y along the x-axis in C1 and the diagonal path (x=y) in C2.

2) Investigate the effects of BCs on reconstruction:

Fig. 5 (last row) compares the reconstructed ECD fields based on formulation with BCs (WBC) and with no BCs (NBC). Table III compares the average (Ave) and standard deviation (SD) of the estimation errors of each iteration, where the α values are listed for completeness.

3) Parametric study on reconstruction robustness:

Gaussian white noise was added into the "measurements" to simulate the effects of sensor noise characterized by a signal-to-noise ratio (SNR). The effects of SNR and the sensor spacing d_s on the regularization parameters and estimation errors (with and without BCs in the formulation) are compared in Table IV and Fig. 6.

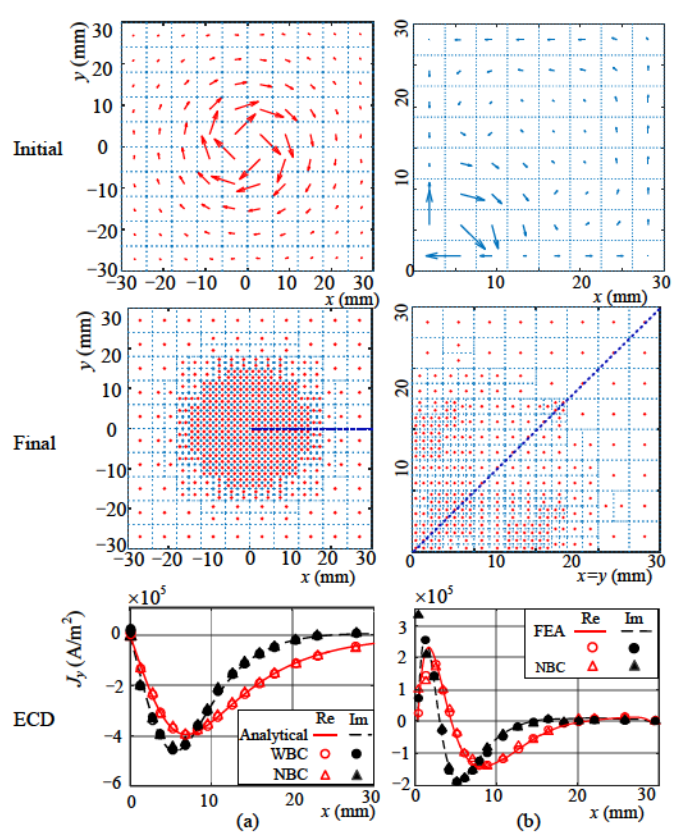


Fig. 5. Verification of ECD reconstruction (a) C1. (b) C2. 1^{st} row: Initial element distribution. 2^{nd} row: Final element distribution. 3^{rd} row: ECD along the *x*-axis and the diagonal (x=y) path.

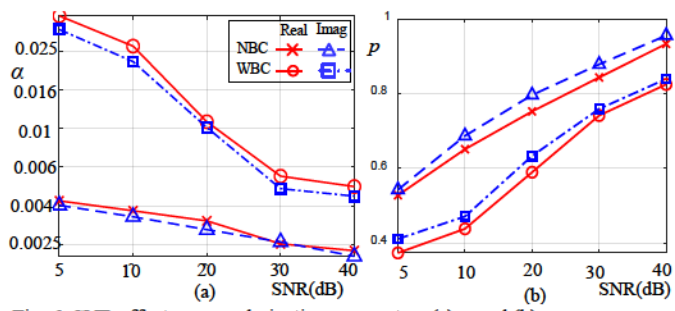


Fig. 6. SNR effects on regularization parameters (a) α and (b) p.

Table III. Estimation errors of each iteration (Ave, SD) (%)

	Cl		C2	2	
Iter	ation	NBC	WBC	NBC	WBC
	α	0.0089	0.0084	0.0063	0.0095
1	Re	-6.74, 19.41	-23.31, 30.17	-73.94, 87.59	-38.42, 84.15
	Im	27.18, 42.50	12.72, 31.93	-35.22, 97.19	-59.62, 109.35
	α	0.0031	0.0039	0.0023	0.0029
2	Re	-9.72, 21.21	-5.19, 11.57	-2.71, 22.68	-3.54, 27.37
	Im	2.08, 6.39	8.28, 12.41	-12.63, 25.37	-15.47, 35.65
	α	0.0008	0.0000	0.0005	0.0000
3	Re	-0.73, 1.95	-0.21, 1.79	2.05, 15.71	-0.68, 4.82
	Im	0.41, 0.78	0.75, 2.92	1.83, 4.74	-1.65, 4.83

Table IV. Effects of SNR and sensors on errors (Ave, SD) (%)

	Effect of SNR on estimation errors, C1						
SNR	(dB)	40	30	20	10	5	
N	Re	0.86, 3.93	1.46, 7.39	5.86, 16.49	5.60, 17.26	8.37, 21.26	
N BC	Im	0.71, 4.85	1.93, 8.36	4.09, 19.38	4.47, 62.31	16.29, 105.98	
w	Re		1.41, 9.93	7.37, 7.92	5.87, 10.05	4.36, 17.04	
BC	Im	0.64, 4.86	2.03, 8.59	5.38, 13.15	5.26, 9.84	6.69, 24.11	

Effe	Effect of sensor configuration (d_s) on estimation errors, C1					
d₅ (mm)	4	6	10	12	15	
a	0.0059	0.0102	0.0132	0.0225	0.0257	
Re	0.73, 1.95	3.85, 4.39	8.47, 9.26	10.32, 17.25	18.36, 14.72	
Im	0.41, 0.78	2.16, 6.61	6.93, 13.73	17.37, 22.52	25.27, 27.94	

Some observations can be drawn from the results:

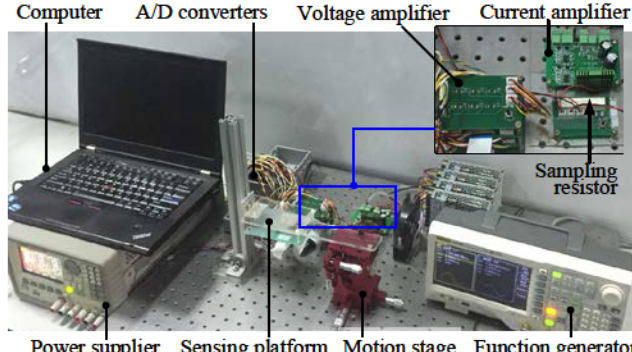
- The adaptive refinements for both C1 and C2 converse to their respective final element distribution after 3 iterations (Fig. 5) with estimation errors in the order of 5% or less (Table III), and α → 0.
- Theoretically, [R_α]→[R] and X_α→X as α → 0. In the absence of noise, the ECD J_y (reconstructed from either NBC or WBC) along the x-axis (or a radial) path of C1 (Fig. 5a) is nearly identical to that calculated from the 2D-axisymmetric analytical solutions. Similarly, the WBC-reconstructed J_y in C2 along the x-y (or diagonal) path about which the ECD J_y is symmetric, closely agrees with FEA in the absence of noise (Fig. 5b). However, some discrepancies between NBC solutions and FEA can be seen when x < 2.5mm, revealing the boundary (corner) effects neglected in the formulation with NBC.</p>
- Fig. 6 and Table IV compare the effects of boundary constraints (NBC and WBC) on estimation errors of the reconstructed ECD fields subjected to measurement noise with the same SNR. Although the estimation can be improved with a larger α that provides more regularization to filter noise in measurements, the additional physical constraints are much more effective to suppress the effects of measurements noise than that without constraints.
- The parameter α and estimation errors decrease as the sensor spacing d_s reduces (Table IV) as expected.
- The parameter p increases with SNR and as regularization parameter α decreases. For all cases illustrated in Fig. 6, the parameter p satisfies the condition 0 .
- The computational time to reconstruct an ECD field increases

with the number of iterations, which represents a tradeoff between time and accuracy. Since the number of elements may increase after each iteration, computational time is not linear with the number of iterations. Using C1 in Table III as an illustration, the calculations to reconstruct one frame of ECD take about 0.137sec, 0.821 sec and 2.793 sec, which correspond to (Re, Im) estimation errors of (-6.74%, 27.18%), (-9.72%, 2.08%) and (-0.73%, 0.41%), for one, two and three iterations respectively.

B. Experimental Investigation

The method of reconstructing a physical field from MFD measurements was experimentally validated on the prototype sensor testbed as illustrated in Fig. 7(a, b) where the test-sample (Al slab) was placed between the stationary sensor board and the EM positioned by a precision 3D motion stage. Three sets of experiments were conducted to demonstrate three applications where the parametric values involved are tabulated in Table V and the results are presented in Figs. 8, 9 and 10, and Table VI:

- Geometric feature detection (Fig. 8)
- Conductivity distribution estimation (Fig. 9)
- ECD field reconstruction (Fig. 10)



Power supplier Sensing platform Motion stage Function generator

Sensor board

Sensor board

Sensor board

Sensor board

Sensor board

MED sensors

(HMC1052)

Computer Sampling resistor

Voltage amplifier

(b)

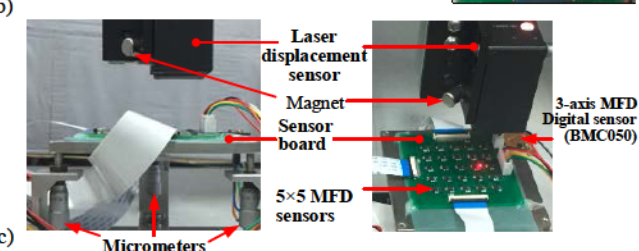


Fig. 7. Experimental setup. (a) Testbed overview. (b) Sensing/ data-acquisition systems. (c) Calibration setup.

The corresponding EC-generated MFD measurements were voltage-amplified before sampled by a (National Instruments) NI data acquisition system (consisting of a cDAQ-9178 with three NI-9205 modules); the sampling rate for each channel was

set to 10 kHz. The sinusoidal current was generated by a function generator and amplified before flowing through the EM, which was determined by measuring the voltage across a sampling resistor connected in series with the EM and sampled through an analog-to-digital (AD) converter. Computations were performed on a computer that communicates with the NI devices through a USB port.

The measurement system consists of 5×5 (2-axis HMC1052) analog MFD sensors evenly spaced ($d_s = 10$ mm) on a printed circuit board (Fig. 7b). Ideally, all sensors should have identical outputs in a uniform magnetic field. Thus, the sensors were individually calibrated using the setup (Fig. 7c) where the sensor board was pre-leveled by three micrometers guided by a laser displacement sensor attached on the precision 3D-motion stage. The individual gain-factor, (g_{xi} , g_{yi}) where i=1, 2, ..., 25, was calibrated using a cylindrical permanent magnet (PM) and a 3-axis magnetic digital sensor (BMC050), which together serve as a referenced pair of input (β_{cx} , β_{cy}) and output (V_{cxi} , V_{cyi}). Mounted on the precision 3D-motion stage, the referenced (PM and digital sensor) pair was positioned above each sensor to determine its gain factor:

$$\begin{bmatrix} g_{xi} \\ g_{yi} \end{bmatrix} = \begin{bmatrix} \beta_x / V_{cxi} \\ \beta_{cy} / V_{cyi} \end{bmatrix}$$
 (23)

Three sets of experiments were conducted to demonstrate the applications; geometric feature detection, conductivity distribution estimation, and ECD field reconstruction. The parametric values involved are tabulated in Table V; and the results are presented in Figs. 8, 9 and 10, and Table VI.

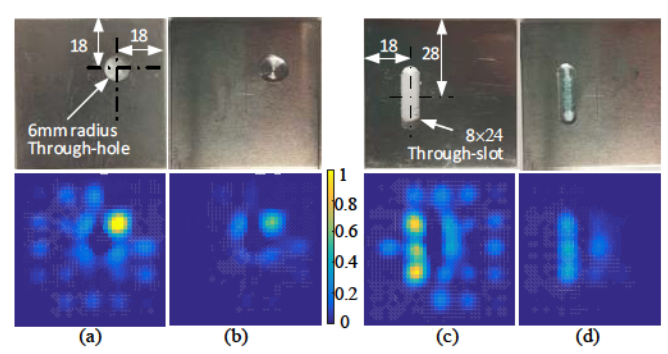


Fig. 8. Experimental detection of geometrical features. (a) Through hole. (b) Blind hole. (c) Through slot. (d) Blind slot.

The color-bar in Fig. 8 (2nd row) represents the value of the elements in the probability vector **T** as shown Eq. (8a), which has a value between 0 (conductive) and 1 (non-conductive) indicating the likelihood that the element is electrically conductive. The experimental results in Fig. 8 demonstrate the detection of four different types of geometrical features (through/blind circular-hole/rectangular-slot), where the depth of both blind features is 1.5mm. The geometrical features can be successfully detected by using MFD measurements. The values of the elements in the through (hole or slot) features are approximately equal to 1 whereas the internal features (blind hole and slot) with values less than 1. Besides the actual features, several "shadows" that have similar shapes as defects appear in the results; however, their intensities are much smaller than that of the actual cavity defects. Inspired by the numerical analysis,

the "shadows" may be introduced by the limitation of measurement number.

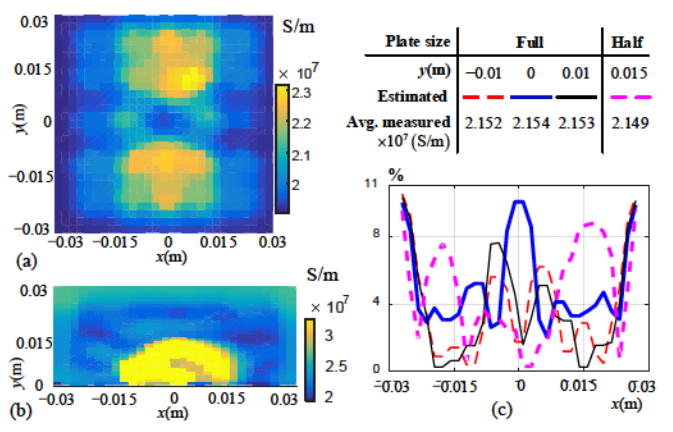


Fig. 9. Conductivity estimation for 6061. (a) Estimated conductivity of full plate. (b) Estimated conductivity of half-plate. (c) Percentage errors of the estimated conductivity along different y. (d) 1D ECD J_y for corner. (e) 1D ECD J_x and J_y for straight edge.

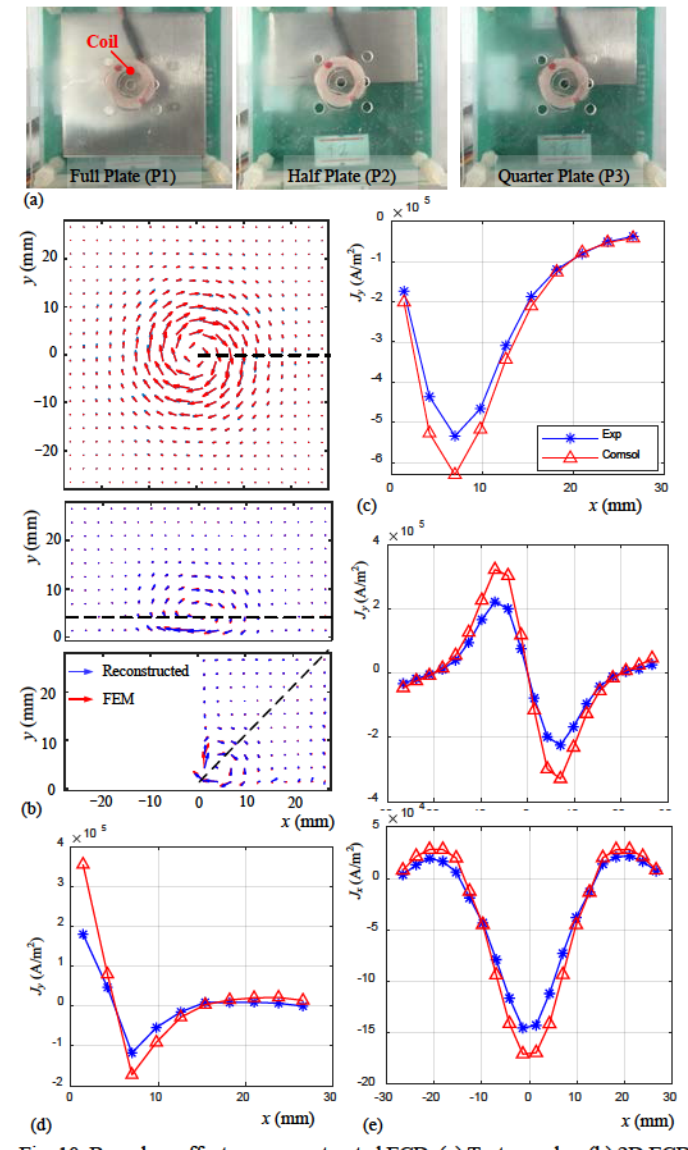


Fig. 10. Boundary effects on reconstructed ECD. (a) Test samples, (b) 2D ECD for axisymmetric/boundary-free, straight edge and corner, (c) 1D ECD J_y for axisymmetric (d) 1D ECD J_y for corner, (e) 1D ECD J_x and J_y for straight edge

Figure 9 displays the estimated conductivity distributions of a full-size plate and a half-size plate, both made of aluminum alloy (Al alloy 6061), respectively. As an illustration, the design assumes a uniform $\overline{\sigma}$ =1.903×10⁷ S/m (for Al alloy 7075); and the actual conductivities were experimentally measured using the Sigma 2008A to provide a basis for experimental verification. Since commercial conductivity gauges can only perform measurements at discrete locations, only 1D conductivity distributions along several lines (y = -10, 0, 10, 15 mm) of the full and half plates were measured. To facilitate visualization, Figs. 9(a) and 9(b) show the conductivities estimated by measuring the EC-generated MFD of the full and half plates. The estimation errors defined in (24) where $\sigma_{\rm est}$ and $\sigma_{\rm meas}$ are the estimated and measured conductivities are plotted in Fig. 9(c):

% error =
$$100 \frac{|\sigma_{\text{est}} - \sigma_{\text{meas}}|}{\sigma_{\text{meas}}}$$
 (24)

The discrepancy between Fig. 8(a) and Fig. 9, which show a circular-symmetric field and a mirror-symmetric appearance respectively, could be due to cumulative errors contributed from both the sensor calibration error and the EC-generated MFD measurement error. In addition, Al alloy 7075 plate used for β measurements may not have uniform conductivity.

Table V Parameters used in experiment (dimension in mm)

100-turn EM: $(a_o, a_o, a) = (6.5, 7.7, 3.65)$. Input: $(I_o = 1 \text{A: } f = 1 \text{ kHz})$ Two-axes Sensors (HMC1052)

 $(N_M; d_s, z_s) = (5 \times 5; 10, -12.5); (LL: d_s: UL) = (-20: 10: 20)$

Al slab $\sigma = 2.16 \times 10^7 \text{ S/m}, z_C = -7.1$

ECD reconstruction: (k, Q, g) = (0.1, 3, 30%)

3mm-thick plates ($w_1 \times w_2$): Full (56×56); Half (56×28); Quarter (28×28) Conductivity **Experiments ECD Feature** (plate thickness) (h=3mm)(h=3 mm) $(h=1 \,\mathrm{mm})$ Element size 5.6×5.6 1.4×1.4 1.86×1.86 400, 200, 100 1600 900 N_E

FEA (COMSOL)simulation parameters					
(Space, total elements, boundary elements, minimum quality)					
P1	80×80×40mm	78361	4561	0.2632	
P2	80×60×40mm	60163	3873	0.2376	
P3	60×60×40mm	47261	2934	0.2012	

Table VI. Physical field estimation errors (%)

Difference between	reconstructed ECD and	d FEA (Ave, SD):
P1. 13.5. 11.4	P2: 18 4 13 5	P3: 25 3 20 5

Estimation errors of feature location and size:

	Circular hole		Rectangular slot	
	Through Blind		Through	Blind
Location: (x, y)	(9.6, 6.2)	(7.0, 5.2)	(6.3, 7.2)	(11.3, 2.3)
Radius or (a, b)	10.4	18.6	(10.5, 5.8)	(3.7, 10.4)

Conductivity estimation errors (Ave, SD):

P1: 6.5, 5.0 **P2**: 8.4, 13.5

Figure 10(a) compares the three different geometrical boundaries relative to the EM and sensor board; no boundary effect (or axisymmetric), straightedge and corner, which are denoted as P1 (full plate), P2 (half plate) and P3 (quarter plate) in Tables V and VI. Plotted in Figs. 10(b, c, d, e) where the three (full, ½ and ¼) plates are evenly divided into 400, 200 and 100 (5.6mm × 5.6 mm) elements respectively, the experimentally reconstructed ECD fields induced in P1, P2 and

P3 (indicated as blue-colored vectors) and the corresponding FEA simulations (red colored vectors) show consistently similar field patterns. Quantitative differences between the reconstructed ECD and FEA are listed in Table VI, where FEA (as a basis for comparisons) computes the ECD field based on the actual experiment setup and the given coil/conductors, while the reconstruction is essentially an inverse problem solving for the ECD field from the limited 5×5 array of MFD measurements. The discrepancy between the experimental estimation and FEA in Fig. 10 can be explained with the aid of Table IV where the effects of system noises and measurement errors on the estimation are numerically analyzed. illustrated in Table IV, an increase of sensor interval d_s , both the regularization parameter α and estimation errors increases. Based on the simulation results in Table IV with the same sensor configuration ($d_s = 10$) as in the experiment setup, the (8.47%, 6.93%) estimation errors of the (Re, Im) simulation are in the same order in the experiments. This discrepancy is within the expectation of the simulations that demonstrate that the accuracy of the reconstructed ECD field can be improved with more sensors (smaller d_s).

IV. CONCLUSION

A new machine perception method based on EC effects to reconstruct physical fields using finite MFD measurements has been presented. The eddy-current and measurement models for physical field reconstruction have been derived in state-space, and formulated as inverse problems, which have been solved using the Tikhonov regularization method. The effectiveness and accuracy of the EC-based machine perception for reconstructing conductivity, hidden geometrical features and ECD have been illustrated numerically and experimentally using a prototype sensor array. Experimental results show that the percentage (average and standard deviation) of the ECD and conductivity field reconstruction are (19.0, 15.1)% and (7.45, 9.3)% respectively. The location and dimension of the hidden geometrical features can be found within 10% average error.

REFERENCES

- C. Bai, H. Xuan, Z. He, Y. Zou, G. Tang, J. Tang, "Research on centrifugal compressor disk containment of auxiliary power unit." *Aerospace Science & Technology*, V. 68, pp. 37-45, 2017.
- [2] M. U. Islam, L. Xue, and G. McGregor. "Process for manufacturing or repairing turbine engine or compressor components." U.S. Patent No. 6,269,540. 7 Aug. 2001.
- [3] W.E. Frazier, "Meal additive manufacturing: A review," J. of Materi. Eng. and Perform., V.23, pp. 1917-1928, 2014.
- [4] B. Vayre, F. Vignat, F. Villeneuve, "Metallic additive manufacturing: State-of-the-art review and prospects," *J. of Mechanics and Industry*, V.13, pp. 89-96, 2012.
- [5] K.-F. Bernard, "Knowledge-based support in Non-Destructive Testing for health monitoring of aircraft structures." *Advanced Engineering Informatics*, V.26, pp. 859-869, 2012.
- [6] N. De Geeter, G. Crevecoeur, L. Dupre, "Eddy-current simulations using an independent impedance method in anisotropic biological tissues," *IEEE Trans. on Magn.*, V.47, no. 10, pp. 3845-3848, 2011.
- [7] K. M. Lee, B. Hao, M. Li, K. Bai, "Multi-parameter eddy-current sensor design for conductivity estimation and simultaneous distance and thickness measurements," *IEEE Trans. on Industrial Informatics*, DOI: 10.1109/TII.2018.2843319, 2018.
- [8] J. C. Moulder, E. Uzal, J. H. Rose, "Thickness and conductivity of

- metallic layers from eddy current measurements," *Review of Scientific Instruments*, V.63, no. 6, pp. 3455-3465,1992.
- [9] F. Sakran, M. Golosovsky, H. Goldberger, D. Davidov, "High-frequency eddy-current technique for thickness measurement of micron-thick conducting layers," *Applied Physics Letters*, V.78, no. 11, pp. 1634-1626, 2001.
- [10] R. Grimberg, L. Udpa, A. Savin, R. Steigmann, V. Palihovici, and S. S. Udpa, "2D eddy current sensor array," NDT & E International, V.39, no. 4, pp. 264-271, 2006.
- [11] R. Grimberg, A. Savin, E. Radu, O. Mihalache, "Nondestructive evaluation of the severity of discontinuities in flat conductive materials by an eddy-current transducer with orthogonal coils," *IEEE Trans. on Magn.*, V.36, no. 1, pp. 299-307, 2000.
- [12] D. G. Park, C. S. Angani, G. D. Kim, C. G. Kim, Y. M. Cheong, "Evaluation of pulsed eddy current response and detection of the thickness variation in the stainless steel," *IEEE Trans. on Magn.*, V.45, no. 10, pp. 3893-3896, 2009.
- [13] J. Kral, R. Smid, H. M. G. Ramos, A. L. Ribeiro, "The lift-off effect in eddy current on thickness modeling and measurement," *IEEE Trans. on Instrum. & Meas.*, V.62, no. 7, pp. 2043-2049, 2013.
- [14] B. A. Abu-Nabah, F. Yu, W. T. Hassan, M. P. Blodgett, P. B. Nagy, "Eddy current residual stress profiling in surface-treated engine alloys," NDT & E International, V.24, nos. 1-2, pp. 209-232, 2009.
- [15] M. Morozov, G. Y. Tian, P. J. Withers, "Noncontact evaluation of the dependency of electrical conductivity on stress for various ai alloys as a function of plastic deformation and annealing,", *J. Appl. Phys.*, V. 108, no. 2, pp. 024909-1-024909-9, 2010.
- [16] X. Ma, A.J. Peyton, Y. Y. Zhao, "Eddy current measurements of electrical conductivity and magnetic permeability of porous metals," NDT & E International, V.39, pp. 562-568, 2006.
- [17] X. Chen, Y. Lei. "Electrical conductivity measurement of ferromagnetic metallic materials using pulsed eddy current method." NDT & E Int., V. 75, pp.33-38, 2015.
- [18] G. Preda, F. I. Hantila, "Nonlinear integral formulation and neural network-based solution for reconstruction of deep defects with pulse eddy currents," *IEEE Trans. on Magn*, V. 50, no. 2, pp. 113-116, 2014.
- [19] J. A. Buck, P. R. Underhill, S. G. Mokros, J. E. Morelli, V. K. Babbar, B. Lepine, T. W. Krause, "Pulsed eddy current inspection of support structures in steam generators," *IEEE Sensors Journal*, V. 15, no. 8, pp. 4305-4312, 2015.
- [20] D. P. Johnston, J. A. Buck, P. R. Underhill, J. E. Morelli, T. W. Krause, "Pulsed eddy-current detection of loose parts in steam generators," *IEEE Sensors Journal*, V. 18, no. 6, pp. 2506-2512, 2018.
- [21] Y. He, R. Yang, X. Wu, S. Huang, "Dynamic scanning electromagnetic infrared thermographic analysis based on blind source separation for industrial metallic damage evaluation," *IEEE Trans. on Industrial Informatics*, V. 14, no. 12, pp. 5610-5619, 2018.
- [22] J. Zhu, Q. Min, J. Wu, G. Y. Tian, "Probability of detection for eddy current pulsed thermography of angular defect quantification," *IEEE Trans. on Industrial Informatics*, V. 14, no. 12, pp. 5658-5666, 2018.
- [23] I. Rubi-Fessen, A. Hartmann, W. Huber, B. Fimm, T. Rommel, A. Thiel, and W. D. Heiss, "Add-on Effects of rTMS on Subacute Aphasia Therapy: Enhanced Improvement of Functional Communication and Basic Linguistic Skills. A Randomized Controlled Study," *Archives of physical medicine and rehabilitation*, V. 96, no. 11, pp. 1935-1944, 2015.
- [24] J. Lim, K.-M. Lee. "Distributed multilevel current models for design analysis of electromagnetic actuators," *IEEE/ASME Trans. on Mech.*, V.20, no. 5, pp. 2413-2424, Oct. 2015.
- [25] C. R. Vogel, Computational method for inverse problems, SIAM, 2002.
- [26] P.C. Hansen, "Numerical Tools for analysis and solution of fredholm integral equations of the first kind," *Inverse Problems*, V. 8, no. 6, pp. 956-972, 1992.
- [27] M. Hanke, P.C. Hansen, "Regularization methods for large-scale problems," *Surveys on Math. for Industry*, V.3, pp.253-315, 1993.
- [28] G. S. Brady, H. R. Clauser, J. A. Vaccari, Materials Handbook, McGraw Hill, 1996.
- [29] C. V. Dodd, W. E. Deeds. "Analytical solutions to eddy-current probecoil problems," J. Appl. Phys., V.39, no.6, pp. 2829-2838, 1968.
- [30] J. W. Luquire, W. E. Deeds. "Alternating current distribution between planar conductors," J. Appl. Phys., V.41, no.10, pp. 3983-3991, 1970.



Min Li received the B.S. and M.S. degrees in mechanical engineering from the Huazhong University of Science and Technology, Wuhan, China, in 2008 and 2011, respectively, and the Ph.D. degree in mechanical engineering from Georgia Institute of Technology, Atlanta, GA, USA in 2017.

He is currently an Assistant Professor with the Department of Mechanical and

Civil Engineering, Minnesota State University, Mankato, MN 56001 USA. His research interests include system dynamics/control, robotics, automation, and mechatronics.



Kok-Meng Lee (M'89–SM'02–F'05) received the B.S. degree in mechanical engineering from the State University of New York, Buffalo, NY, USA, in 1980, and the S.M. and Ph.D. degrees in mechanical engineering from the Massachusetts Institute of Technology, Cambridge, MA, USA, in 1982 and 1985, respectively.

He is currently a Professor with the George W. Woodruff School of

Mechanical Engineering, Georgia Institute of Technology, Atlanta, GA, USA. He is also a Distinguished Professor with the State Key Laboratory of Digital Manufacturing Equipment and Technology, Huazhong University of Science and Technology, Wuhan, China. His research interests include system dynamics/control, robotics, automation, and mechatronics. He holds eight patents in machine vision, three degrees-of-freedom spherical motor/encoder, and live-bird handling system.

Dr. Lee is a life fellow of the American Society of Mechanical Engineers (ASME). He is the founding Editor-in-Chief of Springer International Journal of Intelligent Robotics and Applications. He received the National Science Foundation Presidential Young Investigator, the Sigma Xi Junior Faculty Research, the International Hall of Fame New Technology, the Kayamori Best Paper Awards, the TMech Best Paper Award, and the Michael J. Rabin Leadership Award. He was also honored as a Pao Yu-Kong Chair Professor at Zhejiang University, Hangzhou, China.